

State-Plane-Based Frequency Domain Analysis and Optimal Design for SS Compensated IPT Systems

Yihan Wu¹, Student Member, IEEE, Bo Xue¹, Junrui Liang¹, Senior Member, IEEE, Minfan Fu¹, Senior Member, IEEE, and Haoyu Wang¹, Senior Member, IEEE

Abstract—When modeling series-series (SS) compensated inductive power transfer (IPT) systems, conventional frequency-domain methods focus on output characteristics while neglecting the time-domain information of the current. To improve the model accuracy, we propose a state-plane-based frequency domain analysis method. It integrates both time and frequency information, providing a more comprehensive analysis. By decoupling the coupling coil model, two independent equivalent circuits and their corresponding state-plane diagrams are developed. Hence, the amplitude and phase of each harmonic component can be accurately determined. Additionally, the proposed model allows for the precise calculation of the switch turn-off currents. The study also depicts the zero-voltage-switching (ZVS) ranges under various output conditions. An optimal modulation strategy is developed to minimize the condition losses while ensuring ZVS of all MOSFETs over the entire power range. A 400 W laboratory prototype is built and tested. The experiment results effectively validate the model's accuracy. A 95.61% peak efficiency is recorded with improved performance throughout its operational power range.

Index Terms—Frequency domain, inductive power transfer (IPT), modeling, series-series (SS) compensation, state-plane.

I. INTRODUCTION

INDUCTIVE power transfer (IPT) technology provides a convenient solution to charge battery-powered devices. It has the potential to revolutionize traditional energy utilization across various applications, including mobile electronics devices [1], implanted devices [2], Internet of Things [3], electric vehicles [4], and autonomous aerial vehicles [5], [6]. The IPT system is essentially a resonant converter with a low-coupling coefficient. Establishing the steady-state mathematical model of the resonant converter or IPT system plays a critical role in guiding efficiency optimization, parameter design, and performance evaluation [7], [8].

Received 3 December 2024; revised 16 April 2025; accepted 3 June 2025. Date of publication 10 July 2025; date of current version 21 November 2025. This work was supported by the National Natural Science Foundation of China under Grant 52077140. (Corresponding author: Haoyu Wang.)

The authors are with the School of Information Science and Technology, ShanghaiTech University, Shanghai 201210, China (e-mail: wuyh22023@shanghaitech.edu.cn; xuebo@shanghaitech.edu.cn; liangjr@shanghaitech.edu.cn; fufm@shanghaitech.edu.cn; wanghy@shanghaitech.edu.cn).

Digital Object Identifier 10.1109/TIE.2025.3579068

First-harmonic approximation (FHA) is a simple solution for modeling resonant topologies, which only considers the fundamental components of voltage and current while all higher harmonics are ignored. However, FHA exhibits low accuracy under high-distortion operation, which usually occurs at light load [9], [10]. Many techniques are proposed to improve the accuracy of FHA modeling. In [11], the extended first harmonic analysis is proposed. However, it is based on the assumption that the current in the series resonant tank is sinusoidal, which is invalid in some operating conditions of IPT systems. In [12] and [13], a multiple harmonic analysis is proposed to quantitatively analyze the harmonics. This method considers not only multiple higher harmonics but also individual equivalent loads for each harmonic component. However, the analysis is rather complex.

Time-domain analysis is also investigated to improve the modeling accuracy [14], [15]. The time domain expressions of state variables are obtained over one switching period by solving the state-space equations in each subinterval. In [16] and [17], an in-depth analysis of time-domain equations is conducted for various resonance states, and the gain characteristics over the entire switching frequency (f_s) range are explored. In [18], the time domain system behaviors are investigated when f_s is lower than the resonant frequency, with a focus on its gain characteristics. However, most time-domain methods are not suitable for deriving frequency responses. Additionally, these methods typically provide only numerical solutions, and the information regarding resonant current and voltage is not intuitive.

State-plane analysis (SPA) is a more intuitive time-domain method for the design and analysis of resonant converters [19], [20]. In [21], a general SPA method is proposed for bidirectional CLLC resonant converters. This approach decouples the high-order CLLC resonant network into two independent SRC circuits for analysis. However, the process is relatively complex and lacks universality. Due to the compensation networks on both the transmitter (TX) and receiver (RX) sides in IPT systems, the system order is often higher than third order. Consequently, SPA for IPT systems has been rarely studied. Moreover, SPA only considers the steady-state operation, while it does not consider the frequency response of the system. Table I summarizes a detailed comparison between frequency- and time-domain analysis.

In this article, a novel state-plane-based frequency domain analysis method is proposed for series-series (SS) compensated

TABLE I
COMPARISON OF DIFFERENT MODELING METHODS

Category	Frequency-Domain Methods		Time-Domain Methods	
	FHA	Multiple Harmonics Analysis	Numerical Solutions	State-Space Analysis
Complexity	Simple	Complex	Complex	Moderate
Accuracy	Low	High	Highest	High
Practicality	Convenient	Inconvenient	Inconvenient	Convenient
Generality	High	High	High	Low

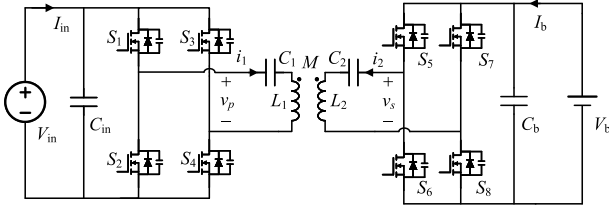


Fig. 1. Schematic of SS compensated IPT system.

IPT systems. Using mathematical methods, we decouple two coupled resonant tanks within an SS compensation circuit into two independent lower order resonant networks. Subsequently, two decoupled equivalent circuits and their corresponding state-plane diagrams are established. The Fourier series expansion of decoupled currents enables accurate extraction of both amplitude and phase information for each harmonic. This approach significantly reduces the complexity of the SS compensation circuit, facilitating topology analysis through the SPA method, which enhances both the accuracy and intuitiveness of the analysis. Furthermore, the integration of frequency-domain analysis streamlines the process of optimizing the circuit's performance.

Subsequently, we utilize the aforementioned modeling and analysis process to optimize the topology for improved performance. The zero-voltage-switching (ZVS) range under various phase shifts and frequency ratios is presented. An optimal modulation scheme is proposed, which reduces conduction losses while ensuring ZVS turn-ON for all MOSFETs across the full power range.

This article is organized as follows. Section II introduces the SS compensated IPT systems. The detailed circuit modeling and derivation are presented in Section III. In Section IV, the optimal parameter design is presented. Section V demonstrates the experimental results. Section VI compares other works in detail and highlights the advantages of this work. Finally, this article concludes in Section VII.

II. SYSTEM DESCRIPTION

The schematic of the SS compensated IPT system is shown in Fig. 1. S_1 – S_4 and S_5 – S_8 are power switches on the primary and secondary sides, respectively. V_{in} is the dc-link voltage, V_b is the battery voltage, v_p and v_s are the inverter voltages of TX and RX sides, respectively. L_1 and L_2 are the self-inductances of TX and RX coils, respectively. C_1 and C_2 are the corresponding compensation capacitance. M is the mutual inductance between

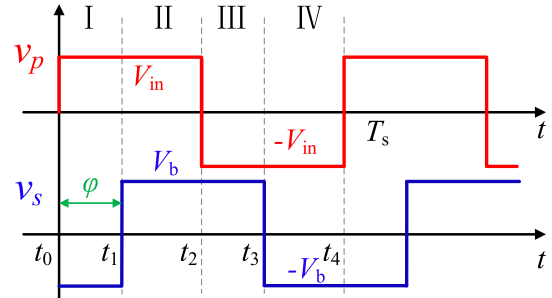


Fig. 2. Voltage waveforms of v_p and v_s .

the TX and RX coils. $M = k\sqrt{L_1L_2}$, where k is the coupling coefficient.

The circuit parameters of the converter are defined as

$$\omega_0 = \frac{1}{\sqrt{L_1C_1}} = \frac{1}{\sqrt{L_2C_2}}, \quad \omega_s = 2\pi f_s = 2\pi/T_s$$

$$L = \sqrt{L_1L_2}, \quad \gamma = \sqrt{L_1/L_2}, \quad r = \frac{\omega_s}{\omega_0}, \quad g = \frac{V_b}{V_{in}} \quad (1)$$

where ω_0 , ω_s , f_s , and T_s are the angular resonant frequency, angular switching frequency, switching frequency, and period. L , γ , r , and g are the characteristics inductance, characteristics inductance ratio, frequency ratio, and voltage gain, respectively.

The modulation strategies of the IPT system can be divided into phase shift modulation and variable frequency modulation. Considering the influence of f_s , without increasing control complexity, only single-phase shift modulation, where there is a phase shift between the TX and RX sides, is considered in this article. In most cases, variable frequency single-phase shift modulation can realize the control target of the IPT systems.

Fig. 2 exhibits the steady-state waveforms of v_p and v_s in variable frequency single phase shift modulation, T_s is the switching period, φ is the phase shift between v_p and v_s . Via maneuvering φ and T_s , the inverter voltage magnitude and phase are actively adjusted to achieve the required power flow.

III. MATHEMATICAL MODELING

To simplify the modeling, the following assumptions are made.

- 1) All passive components and active switches are ideal with zero equivalent series resistance.
- 2) The voltages of the dc-link and the battery are constant.
- 3) The effects of dead time and the output voltage rise/drop time of the full bridge are ignored.

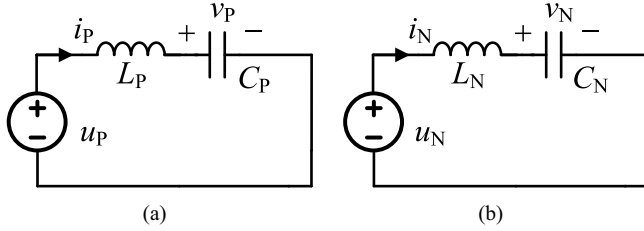


Fig. 3. Equivalent circuit: (a) SRC-P; and (b) SRC-N.

A. Decoupling Analysis

Inductor currents and capacitor voltages i_1, i_2, v_1 , and v_2 are defined as the state variables. Define $\mathbf{u} = [v_p(t); v_s(t)]$, $\mathbf{v} = [v_1(t); v_2(t)]$, and $\mathbf{i} = [i_1(t); i_2(t)]$ as the input voltage vector, capacitor voltage vector, and current vector, respectively. The circuit model can be established as

$$\begin{cases} \mathbf{R}\mathbf{i}' + \mathbf{v} = \mathbf{u} \\ \mathbf{i} = \mathbf{C}\mathbf{v}' \end{cases} \quad (2)$$

where \mathbf{R} and \mathbf{C} are the inductance matrix and capacitance matrix and are defined as

$$\mathbf{R} = \begin{bmatrix} L_1 & M \\ M & L_2 \end{bmatrix}, \quad \mathbf{C} = \begin{bmatrix} C_1 & \\ & C_2 \end{bmatrix}. \quad (3)$$

According to the matrix theory, nonsingular matrices \mathbf{k}_i and \mathbf{k}_v satisfy the following equation:

$$\begin{cases} \mathbf{L}_D = \mathbf{k}_v \mathbf{R} \mathbf{k}_i^{-1} \\ \mathbf{C}_D = \mathbf{k}_i \mathbf{C} \mathbf{k}_v^{-1} \end{cases} \quad (4)$$

where $\mathbf{L}_D = \text{diag}\{L_P, L_N\}$, $\mathbf{C}_D = \text{diag}\{C_P, C_N\}$ and

$$\mathbf{k}_i = \begin{bmatrix} 1 & -1/\gamma \\ \gamma & 1 \end{bmatrix}, \quad \mathbf{k}_v = \begin{bmatrix} 1 & -\gamma \\ 1/\gamma & 1 \end{bmatrix}. \quad (5)$$

Using linear transformation $\mathbf{i}_D = \mathbf{k}_i \mathbf{i}$, $\mathbf{v}_D = \mathbf{k}_v \mathbf{v}$, and $\mathbf{u}_D = \mathbf{k}_v \mathbf{u}$, the coupled state-space model in (2) can be decoupled into two mutually independent equations

$$\begin{cases} \mathbf{L}_D \mathbf{i}_D' + \mathbf{v}_D = \mathbf{u}_D \\ \mathbf{i}_D = \mathbf{C}_D \mathbf{v}_D' \end{cases} \quad (6)$$

where $\mathbf{u}_D = [u_P; u_N]$, $\mathbf{v}_D = [v_P; v_N]$, and $\mathbf{i}_D = [i_P; i_N]$ are the input voltage vector, voltage vector, and current vector of the decoupled model (6). Since matrices \mathbf{L}_D and \mathbf{C}_D are nonsingular, i_P and i_N are independent of each other.

B. SPA

As shown in Fig. 2, since v_p and v_s are piecewise constant, u_P and u_N are piecewise constant. Fig. 3(a) and 3(b) represents the equivalent circuits described by (6), which are denoted by the P-type series resonant converter (SRC-P) and the N-type series resonant converter (SRC-N), respectively. The equivalent circuit parameters are listed in Table II. It can be seen that the BIPT system can be modeled by two independent series resonant converters.

TABLE II
EQUIVALENT CIRCUIT PARAMETERS

L_P	C_P	u_P	L_N	C_N	u_N
$(1-k)L_1$	C_1	$v_p - \gamma v_s$	$(1+k)L_2$	C_2	$v_p/\gamma + v_s$

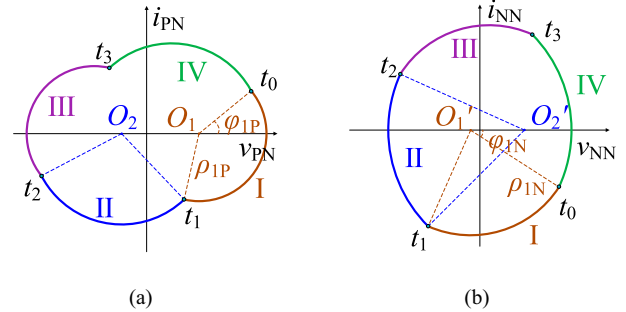


Fig. 4. State-plane diagram of the equivalent circuits: (a) SRC-P; and (b) SRC-N.

The equivalent angular frequencies and characteristic impedances of SRC-P and SRC-N are defined as

$$\begin{aligned} \omega_P &= \frac{1}{\sqrt{L_P C_P}}, & Z_P &= \omega_P L_P \\ \omega_N &= \frac{1}{\sqrt{L_N C_N}}, & Z_N &= \omega_N L_N. \end{aligned} \quad (7)$$

The normalized equivalent voltage and current $\mathbf{u}_{DN} = \{V_{PN}; V_{NN}\}$, $\mathbf{v}_{DN} = \{v_{PN}; v_{NN}\}$, and $\mathbf{i}_{DN} = \{i_{PN}; i_{NN}\}$ are defined as

$$\begin{aligned} \mathbf{u}_{DN} &= \mathbf{V}_{\text{base}}^{-1} \mathbf{u}_D \\ \mathbf{v}_{DN} &= \mathbf{V}_{\text{base}}^{-1} \mathbf{v}_D \\ \mathbf{i}_{DN} &= \mathbf{I}_{\text{base}}^{-1} \mathbf{i}_D \end{aligned} \quad (8)$$

where

$$\mathbf{V}_{\text{base}} = \begin{bmatrix} V_{\text{in}} & \\ & V_b \end{bmatrix}, \quad \mathbf{I}_{\text{base}} = \begin{bmatrix} V_{\text{in}}/Z_P & \\ & V_b/Z_N \end{bmatrix}. \quad (9)$$

In mode I, v_p is V_{in} and v_s is $-V_b$, the normalized equivalent input voltage $V_{PN1} = 1 + g\gamma$ and $V_{NN1} = 1/(g\gamma) - 1$. The solution is expressed by

$$\begin{cases} i_{PN} = \rho_{1P} \sin(\varphi_{1P} - \omega_P t) \\ v_{PN} = \rho_{1P} \cos(\varphi_{1P} - \omega_P t) + V_{PN1} \\ i_{NN} = \rho_{1N} \sin(\varphi_{1N} - \omega_N t) \\ v_{NN} = \rho_{1N} \cos(\varphi_{1N} - \omega_N t) + V_{NN1} \end{cases} \quad (10)$$

where ρ_{1P} and φ_{1P} are the initial magnitude and phase for SRC-P in mode I. The trajectory of SRC-P and SRC-N are arcs centered at $(V_{PN1}, 0)$ and $(V_{NN1}, 0)$, respectively.

In mode II, v_p is V_{in} and v_s is V_b , the normalized resonant voltage and current are the same as mode I, the only difference is that the input voltage excitation is different, which results in a different center of the circle.

From Table II and (8), the normalized input voltage excitations are different for SRC-P and SRC-N in the same mode, which means the center of the circle of trajectory curves is different. Fig. 4 shows the state-plane diagram of SRC-P and SRC-

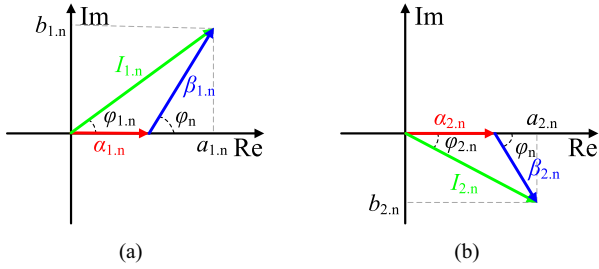


Fig. 5. Phasor diagrams of harmonic components: (a) $I_{1,n}$; and (b) $I_{2,n}$.

N . O_1 (O'_1) and O_2 (O'_2) are the centers of modes I and II in SRC-P (SRC-N), respectively.

C. Frequency Characteristics

According to (6) and Fig. 4, the coupled i_1 and i_2 are decoupled into two independent equivalent currents i_{PN} and i_{NN} . The frequency characteristics of the decoupled i_{PN} are analyzed first. The equivalent inductor current i_{PN} over one switching period is expressed as

$$i_{PN} = \begin{cases} \rho_1 \sin(\varphi_1 - \omega_p t), & t \in (t_0, t_1) \\ \rho_2 \sin(\varphi_2 - \omega_p t), & t \in (t_1, t_2) \\ \rho_3 \sin(\varphi_3 - \omega_p t), & t \in (t_2, t_3) \\ \rho_4 \sin(\varphi_4 - \omega_p t), & t \in (t_3, t_4) \end{cases} \quad (11)$$

where $\rho_i, \varphi_i, i \in \{1, 2, 3, 4\}$ are the initial magnitude and phase for different modes.

The Fourier series expansion of i_{PN} is as follows:

$$i_{PN}(t) = \sum_{n=2k-1}^{\infty} a_{n,P} \cos(n\omega_s t) + b_{n,P} \sin(n\omega_s t) \quad (12)$$

where

$$\begin{cases} a_{n,P} = \frac{2\omega_p \omega_s}{\pi(\omega_p^2 - n^2 \omega_s^2)} [(V_{PN2} - V_{PN1}) \cos \varphi_n \\ + (V_{PN2} + V_{PN1})] \\ b_{n,P} = \frac{2\omega_p \omega_s}{\pi(\omega_p^2 - n^2 \omega_s^2)} (V_{PN2} - V_{PN1}) \sin \varphi_n \end{cases} \quad (13)$$

where $\varphi_n = n\varphi$ is the phase shift of n times harmonic components.

As shown in (12) and (13), i_{PN} is related to the voltage of modes I and II and φ . Similarly, the current of i_{NN} in model SRC-N can be obtained. Substitute $\mathbf{i}_{DN} = [i_{PN}; i_{NN}]$ into $\mathbf{i} = \mathbf{k}_1^{-1} \mathbf{I}_{\text{base}} \mathbf{i}_{DN}$, the TX and RX coil currents are as follows:

$$\begin{cases} i_1 = \sum_{n=2k-1}^{\infty} I_{1,n} \cos(n\omega_s t - \varphi_{1,n}) \\ i_2 = \sum_{n=2k-1}^{\infty} I_{2,n} \cos(n\omega_s t' - \varphi_{2,n}) \end{cases} \quad (14)$$

where $\omega_s t' = \omega_s t - \varphi$, $I_{1,n}, I_{2,n}$, and $\varphi_{1,n}, \varphi_{2,n}$ are the magnitude and phase of harmonic components on the TX and RX sides, respectively. The phasor diagrams of $I_{1,n}$ and $I_{2,n}$ are shown in Fig. 5, $\alpha_{1,n}, \beta_{1,n}, \alpha_{2,n}$, and $\beta_{2,n}$ satisfy the following:

$$\begin{cases} \alpha_{1,n} = (1 - n^2 r^2) I_{0,n} V_{\text{in}} / \gamma \\ \beta_{1,n} = kn^2 r^2 I_{0,n} V_{\text{b}} \end{cases}, \begin{cases} \alpha_{2,n} = (1 - n^2 r^2) I_{0,n} \gamma V_{\text{b}} \\ \beta_{2,n} = kn^2 r^2 I_{0,n} V_{\text{in}} \end{cases} \quad (15)$$

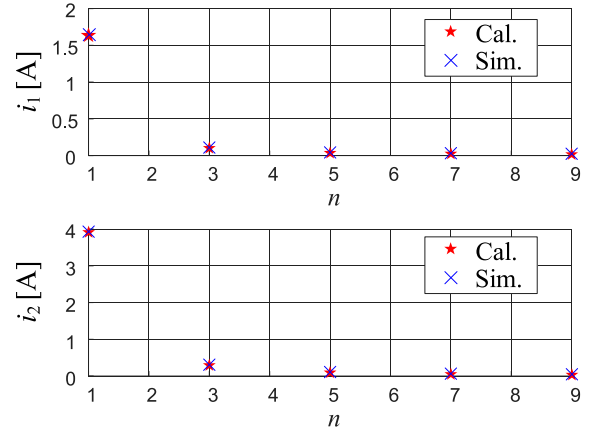


Fig. 6. Calculated and simulated results of harmonic components of TX and RX coil currents.

where $r_1 = 1/\sqrt{1-k}$, $r_2 = 1/\sqrt{1+k}$ and

$$I_{0,n} = \frac{2\sqrt{2}r}{(1-k^2)(n^2 r^2 - r_1^2)(n^2 r^2 - r_2^2)\pi\omega_0 L}. \quad (16)$$

From (15) and (16) $\alpha_{1,n}, \beta_{1,n}$ and $\alpha_{2,n}, \beta_{2,n}$ are independent of phase shift φ and determined by the frequency ratio r . In the special case of $r = r_{1,2}$, the system is unstable. $\beta_{1,n}$ and $\beta_{2,n}$ are negative at $r \in (r_1, r_2)$ and positive in other cases.

Define the output power (P_o) as the power transmitted from the dc link to the battery, the power transfer direction is forward if $P_o > 0$ while backward if $P_o < 0$

$$P_o = \sum_{n=2k-1}^{\infty} \frac{2\sqrt{2}V_{\text{in}}}{n\pi} b_{1,n} = - \sum_{n=2k-1}^{\infty} \frac{2\sqrt{2}V_{\text{b}}}{n\pi} b_{2,n}. \quad (17)$$

The switches turn-OFF currents are as follows:

$$\begin{aligned} I_{S_{1,4}} &= i_1(t_0) = \sum_{n=2k-1}^{\infty} \sqrt{2} a_{1,n} \\ I_{S_{5,8}} &= i_2(t_1) = \sum_{n=2k-1}^{\infty} \sqrt{2} a_{2,n}. \end{aligned} \quad (18)$$

According to (17) and (18) and Fig. 5, $b_{1,n}$ and $b_{2,n}$ correspond to the output power, while $a_{1,n}$ and $a_{2,n}$ correspond to the turn-OFF current.

Fig. 6 shows the calculation and simulation results of harmonic components of TX and RX side currents with $r = 2, \varphi = \pi/3$ condition. As shown, the calculated results match well with simulation results for all harmonic components, which validate the model's accuracy.

Fig. 7 illustrates the comparison between simulation and calculation results for switch current i_{S1} and resonant capacitor current i_{S5} under different f_n values. In the figure, the blue line represents the calculation results from the FHA method, the red line represents the calculation results from our proposed SPA model, and the red pentagram markers represent simulation results. The figure clearly shows that under full-phase-shift conditions, the SPA model's calculation results exhibit higher consistency with simulation results.

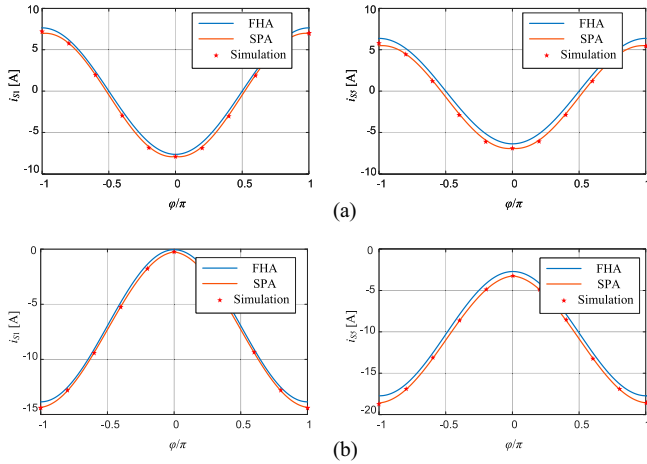


Fig. 7. FHA versus SPA calculation results, and simulation results for i_{S1} and i_{S5} under different f_n values.

IV. OPTIMAL DESIGN

A. Power Characteristics

From (17), the output power is the sum of the power of each harmonic component. The output power of each harmonic is maximum at $\varphi_n = \pi/2$. Defined maximal third harmonic power ratio k_{13} as

$$k_{13} = \frac{b_{1.3}/3}{b_{1.1}} = \frac{3(1-k^2)r^4 - 6r^2 + 3}{81(1-k^2)r^4 - 18r^2 + 1}. \quad (19)$$

k_{13} versus r with different k are shown in Fig. 8, as shown, k has little impact on k_{13} in low- and high-frequency bands. Moreover, the third harmonic power accounts for a relatively large proportion in the low-frequency band and cannot be ignored. k_{13} is lower than 5% when $r > 0.75$, in which case the third harmonic is negligible. Therefore, only the case of $r > 0.75$ is considered, which simplifies the analysis by considering only the fundamental power.

The output power is approximately the fundamental power

$$P_o \approx \frac{2\sqrt{2}V_{in}}{\pi} b_{1.1} = \frac{2\sqrt{2}V_{in}}{\pi} \beta_{1.1} \sin(\varphi). \quad (20)$$

When $r \in (r_1, r_2)$, $\beta_{1.1}$ is negative, $P_o > 0$, $\varphi < 0$ and $P_o < 0$, $\varphi > 0$. In other cases, $\beta_{1.1}$ is positive, $P_o > 0$, $\varphi > 0$ and $P_o < 0$, $\varphi < 0$. The output power reaches its maximum at $\varphi = \pm\pi/2$.

B. ZVS Analysis

The switches turn-OFF current directly affects the ZVS condition. Since the third harmonic power can be ignored, only the fundamental harmonic component of the turn-OFF current is considered to simplify analysis. In most cases, the condition of ZVS turn-ON is that there is a negative turn-OFF current for ease of analysis. According to (18) and Fig. 5, the ZVS turn-ON is achieved when the current falls in the left half plane of current phasor diagrams.

Define $g_\gamma = g\gamma$, the relationship of $\alpha_{1.1}$ ($\alpha_{2.1}$) and $\beta_{1.1}$ ($\beta_{2.1}$) satisfy the following:

$$\begin{cases} |\alpha_{1.1}| < |\beta_{1.1}| \iff 1/\sqrt{1+g_\gamma k} < r < 1/\sqrt{1-g_\gamma k} \\ |\alpha_{2.1}| < |\beta_{2.1}| \iff 1/\sqrt{1+k/g_\gamma} < r < 1/\sqrt{1-k/g_\gamma}. \end{cases} \quad (21)$$

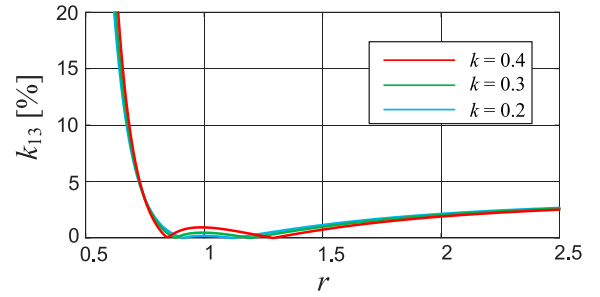


Fig. 8. k_{13} Versus r with different k .

When $g_\gamma \geq 1$,

$$\begin{cases} 1/\sqrt{1+g_\gamma k} < r_1 < 1/\sqrt{1+k/g_\gamma} \\ 1/\sqrt{1-k/g_\gamma} < r_2 < 1/\sqrt{1-g_\gamma k}. \end{cases} \quad (22)$$

According to (21) and (22), there are six different frequency ranges for both TX and RX sides, and each range corresponds to a phase diagram. The current phasor diagrams for different r conditions are shown in Fig. 9. As shown, since $\beta_{1.n}$ and $\beta_{2.n}$ are negative in the range of $r \in (r_1, r_2)$, the shift in the phasor diagram in that range should increase by π . Note that for all r conditions, as φ increases, i_1 rotates clockwise while i_2 rotates counterclockwise.

As shown in Fig. 9, the ZVS range for TX and RX sides is symmetric at the origin, and only the ZVS range of $r \in [0, \pi]$ is considered to simplify the analysis. The ZVS ranges of TX and RX sides are summarized as

$$\varphi_T = \begin{cases} \emptyset, & \text{if } r < 1/\sqrt{1+g_\gamma k} \\ (\pi - \varphi_{ab1}, \pi), & \text{if } r \in (1/\sqrt{1+g_\gamma k}, r_1) \\ (0, \pi - \varphi_{ab1}), & \text{if } r \in (r_1, r_2) \\ (\pi - \varphi_{ab1}, \pi), & \text{if } r \in (r_2, 1/\sqrt{1-g_\gamma k}) \\ (0, \pi), & \text{if } r > 1/\sqrt{1-g_\gamma k} \end{cases}$$

$$\varphi_R = \begin{cases} \emptyset, & \text{if } r < r_1 \\ (0, \pi), & \text{if } r \in (r_1, 1/\sqrt{1+k/g_\gamma}) \\ (0, \pi - \varphi_{ab2}), & \text{if } r \in (1/\sqrt{1+k/g_\gamma}, 1/\sqrt{1-k/g_\gamma}) \\ \emptyset, & \text{if } r \in (1/\sqrt{1-k/g_\gamma}, r_2) \\ (0, \pi), & \text{if } r > r_2 \end{cases} \quad (23)$$

where

$$\varphi_{ab1} = \arccos \frac{1/r^2 - 1}{g_\gamma k}, \quad \varphi_{ab2} = \arccos \frac{1/r^2 - 1}{k/g_\gamma}. \quad (24)$$

For $g_\gamma < 1$, the ZVS range is the same as $g_\gamma \geq 1$ condition.

In summary, the full ZVS range is summarized as

$$\varphi_F = \begin{cases} (\varphi_1 - \pi, \pi - \varphi_1), & \text{if } r \in (r_1, 1) \\ (\varphi_2 - \pi, \pi - \varphi_2), & \text{if } r \in (1, 1/\sqrt{1-g_0 k}) \\ (-\pi, \varphi_1 - \pi) \cup (\pi - \varphi_1, \pi), & \text{if } r \in (r_2, 1/\sqrt{1-k/g_0}) \\ (-\pi, \pi) & \text{if } r > 1/\sqrt{1-k/g_0}. \end{cases} \quad (25)$$

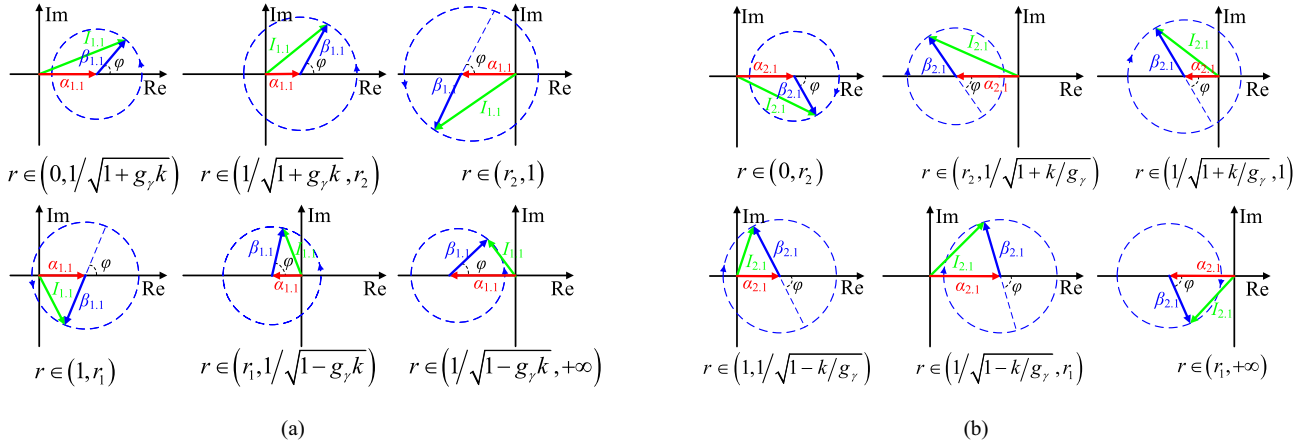


Fig. 9. Current phasor diagrams for different r with $g_\gamma \geq 1$ condition: (a) i_1 ; and (b) i_2 .

where g_0 , φ_1 , and φ_2 are as follows:

$$g_0 = \begin{cases} g_\gamma, & \text{if } g_\gamma < 1 \\ 1/g_\gamma, & \text{if } g_\gamma \geq 1 \end{cases}, \quad \begin{cases} \varphi_1 = \arccos \frac{1/r^2 - 1}{k/g_0} \\ \varphi_2 = \arccos \frac{1/r^2 - 1}{g_0 k} \end{cases} \quad (26)$$

The full ZVS range is related to g_0 and r ; there are two different sets of g_γ with the same ZVS range. Fig. 12 shows the full ZVS range versus r with different g_0 . As shown, with the increase of g_0 , the non-ZVS range squeezes, and the ZVS range expands. All MOSFETs realize full range ZVS turn ON when $r > 1/\sqrt{1-k/g_0}$.

C. Minimize Current Stress

Fig. 10 shows the phasor diagrams of $I_{1,1}$ over the full ZVS range with different r . As shown, two different phase shifts correspond to the same output power in many cases. To minimize the current stress, the phase shift with the real part of the phasor diagram near the origin is selected.

For $r \in (r_1, 1)$, there are the same output power range for $\varphi \in (\varphi_1, \pi/2)$ and $(\pi/2, \pi - \varphi_1)$, but $I_{1,1}$ of $\varphi \in (\pi/2, \pi - \varphi_1)$ less than when $\varphi \in (\varphi_1, \pi/2)$. Therefore, the optimized phase shift range for minimize $I_{1,1}$ with $r \in (1/\sqrt{1+k}, 1)$ is $\varphi \in (0, \varphi_1) \cup (\pi/2, \pi - \varphi_1)$.

For other r cases, the optimized phase shift range is similar to the above and shown in the blue curve in Fig. 10.

To improve the system efficiency, an optimized modulation scheme is proposed to reduce the conduction loss. The total rms current I_{rms} is defined as

$$I_{rms} = \sqrt{I_{1,1}^2 + I_{2,1}^2}. \quad (27)$$

The relationship between I_{rms} , φ , and r is illustrated in Fig. 11, where the curves represent the contours at different power levels. The 2-D projection of I_{rms} in the φ - r plane is shown in Fig. 12. As shown in Fig. 12(a), there are two points P_1 and P'_1 outputs 100 W with ZVS implemented. According to Fig. 12(a), at the same frequency condition, the current stress at P_1 is lower than P'_1 . With the increase of P_o , the frequency range

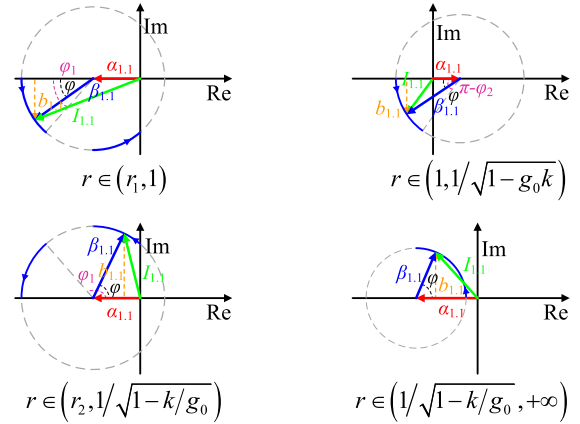


Fig. 10. Phasor diagrams of $I_{1,1}$ over full ZVS range with different r .

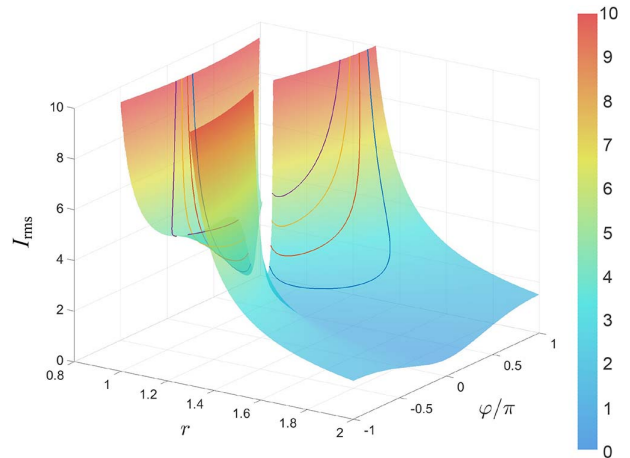
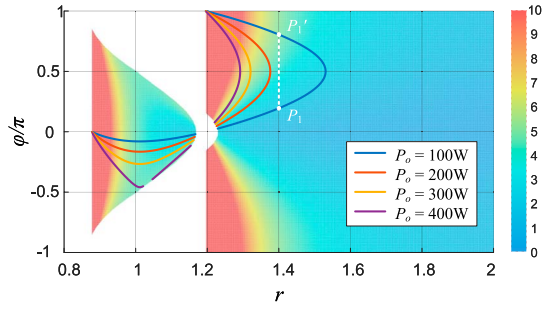


Fig. 11. I_{rms} Surface with power contours versus r and φ ($g = 1$).

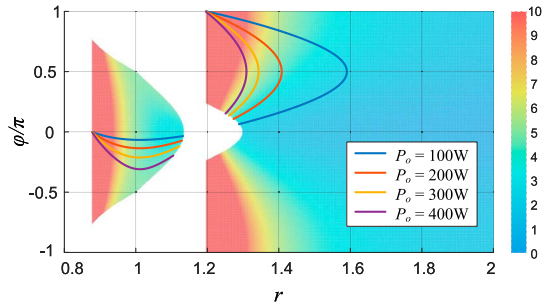
decreases. The frequency range is very narrow at 500 W output condition, the maximal output is set to 400 W.

Fig. 13 shows I_{rms} versus r with different P_o over full ZVS conditions. As shown, different g and P_o correspond to different ZVS ranges and different r and φ . With the increase of P_o , the frequency range decreases. In the special case of $r = 1$, I_{rms} is independent of P_o .

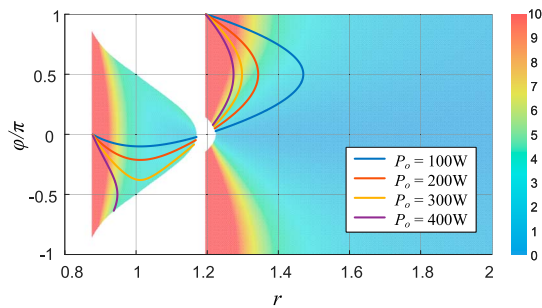
As shown in Fig. 13, different P_o and g correspond to different minimum I_{rms} points (r and φ). The minimum I_{rms} points for



(a)



(b)



(c)

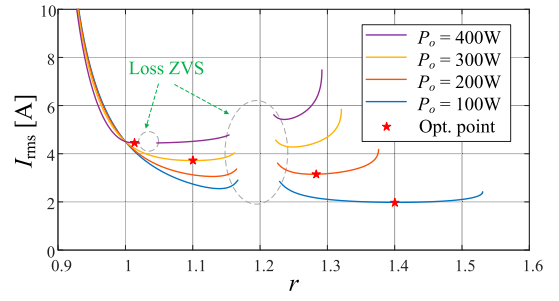
Fig. 12. Curves of φ versus r with different P_o and g : (a) $g = 1$; (b) $g = 1.2$; and (c) $g = 0.8$.

different P_o are marked in Fig. 13 and listed in Table III. As shown, r and I_{rms} decrease as P_o increases.

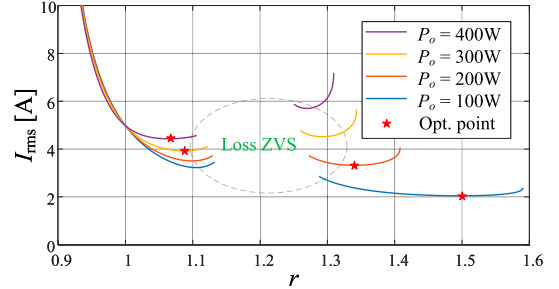
D. Discussion on the Rising/Dropping Time Effect

Practically, due to the rise/drop time of the voltage, v_p and v_s are not ideal square waves. The dead time may affect the phase of v_p and v_s . The rise/drop times of the voltage are determined by the turn-OFF current. Fig. 14 shows the voltage transition scenarios in the dead time. As shown, φ_0 is the control phase shift, and φ is the actual phase shift. There is an error $\varphi_{er} = \varphi - \varphi_0$. t_{d1} and t_{d2} are determined by the turn-OFF resistor of the driver and are approximately equal. t_{off1} and t_{off2} are determined by the turn-OFF current of MOSFETs and output capacitors C_{oss} of MOSFETs

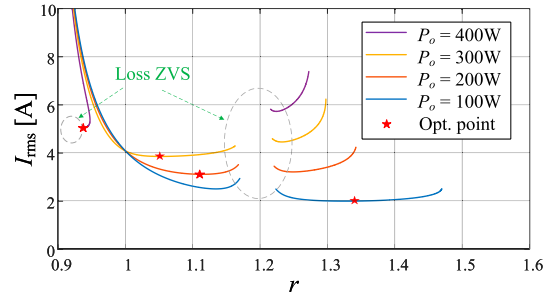
$$t_{off1} = \frac{2C_{oss}V_{in}}{I_{S_{1,4}}}, \quad t_{off2} = \frac{2C_{oss}V_b}{I_{S_{5,8}}}. \quad (28)$$



(a)



(b)



(c)

Fig. 13. I_{rms} versus r with different P_o and g : (a) $g = 1$; (b) $g = 1.2$; and (c) $g = 0.8$.

and

$$\begin{aligned} \varphi_{er} &= \frac{t_{off1} - t_{off2}}{2T_s} \\ &= [g/I_{S_{5,8}} - 1/I_{S_{1,4}}]rC_{oss}V_{in}f_0. \end{aligned} \quad (29)$$

The actual φ is $\varphi = \varphi_0 + \varphi_{er}$. From (28), φ_{er} is related to the turn-OFF current, voltage ratio g , and switching frequency ratio r .

V. EXPERIMENTAL VALIDATIONS

A prototype of the SS compensated IPT system is shown in Fig. 15. The switching transistors and driver chips are Infineon's BSC220N20NSFD and 2EDS8265H, respectively. The controller model is TMS320F28335. Since this article focuses primarily on the modeling and analysis of IPT systems, a single set of controllers is shared by the TX and RX sides to simplify the complexity of control. The detailed parameters of the coil

TABLE III
OPTIMAL PARAMETERS WITH MINIMAL I_{rms}

P_o [W]	$g = 0.8$			$g = 1.0$			$g = 1.2$		
	r	φ	I_{rms} [A]	r	φ	I_{rms} [A]	r	φ	I_{rms} [A]
100	1.33	0.144π	2.81	1.40	0.195π	2.76	1.50	0.269π	2.88
200	1.11	-0.132π	4.38	1.28	0.145π	4.45	1.34	0.225π	4.70
300	1.05	-0.336π	5.44	1.10	-0.182π	5.26	1.09	-0.161π	5.54
400	0.94	-0.636π	7.13	1.02	-0.450π	6.28	1.06	-0.272π	6.26

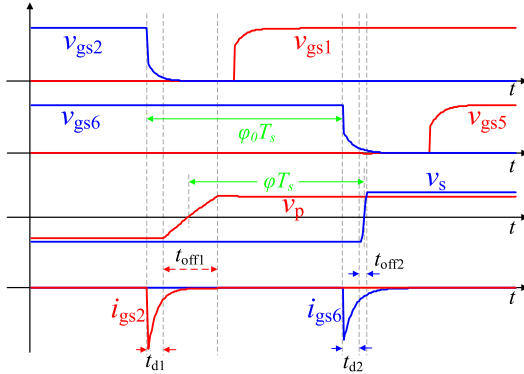


Fig. 14. Voltage transition scenarios in the dead time.

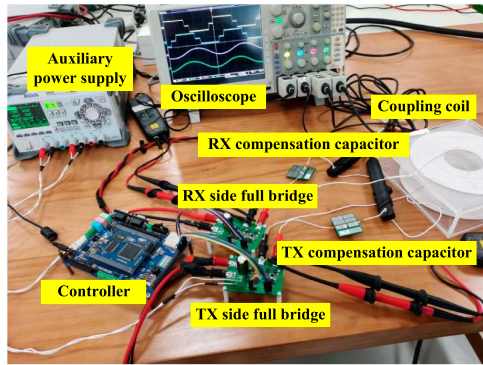


Fig. 15. Experimental prototype of SS compensated IPT systems.

TABLE IV
COIL PARAMETERS

Coil Parameters	TX Coil	RX Coil
Number of Turns	30	27
Litz Wire Diameter (mm)	2	2
Outer Diameter of Coil (mm)	192	174
Inner Diameter of Coil (mm)	60	60
Coil Self-Inductance (μ H)	119.3	94.1
Coil Parasitic Resistance (Ω)	0.15	0.13
Air Gap Distance (mm)	48	
Coupling Coefficient	0.3	

structure are shown in Table IV, and its appearance is shown in Fig. 16.

A 400 W prototype with 100 V input is designed. The key experimental parameters are: $f_0 = 100$ kHz, $L_1 = 119.3$ μ H,

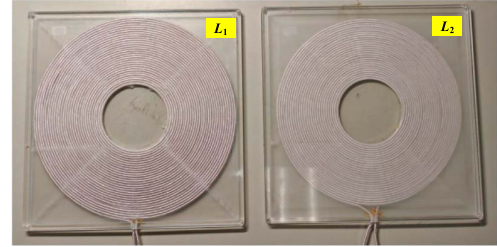


Fig. 16. Coil structure.

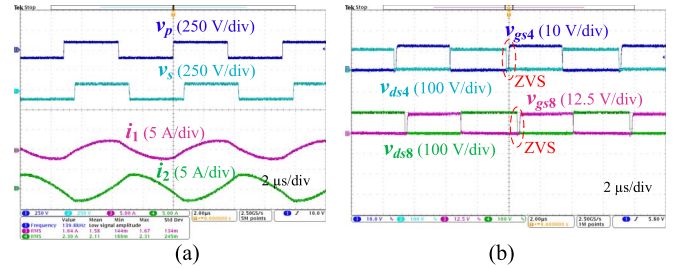


Fig. 17. Experimental steady-state waveforms with $g = 1.0$, $P_o = 100$ W: (a) v_p , v_s , i_1 and i_2 ; and (b) v_{gs4} , v_{ds4} , v_{gs8} , v_{ds8} .

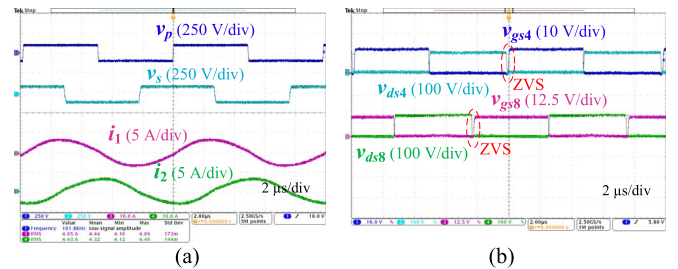


Fig. 18. Experimental steady-state waveforms with $g = 1.0$, $P_o = 400$ W: (a) v_p , v_s , i_1 and i_2 ; and (b) v_{gs4} , v_{ds4} , v_{gs8} , v_{ds8} .

$L_2 = 94.1$ μ H, $C_1 = 21.2$ nF, $C_2 = 26.9$ nF, and $k = 0.3$. All experimental modulation parameters are summarized in Table III (where $f_n = f_s/f_0$).

Figs. 17 and 18 show the steady-state waveforms with 100 and 400 W outputs at $g = 1.0$, respectively. As shown, with the increase of P_o , r increases, and the phase shift φ changes from leading to lagging. Both TX and RX sides achieve ZVS turn-ON.

The waveforms with different P_o at $g = 1.2$ and $g = 0.8$ are shown in Figs. 19 and 20 and Figs. 21 and 22. As shown, the proposed method achieves ZVS on both sides in all output conditions.

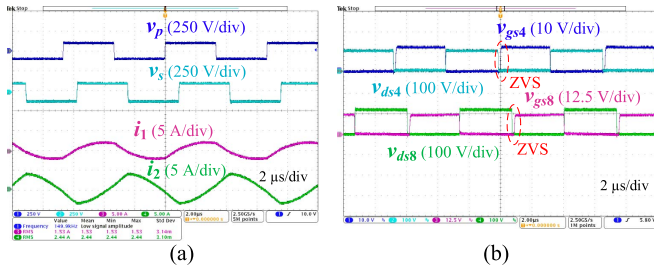


Fig. 19. Experimental steady-state waveforms with $g = 1.2, P_o = 100W$: (a) v_p, v_s, i_1 and i_2 ; and (b) $v_{gs4}, v_{ds4}, v_{gs8}, v_{ds8}$.

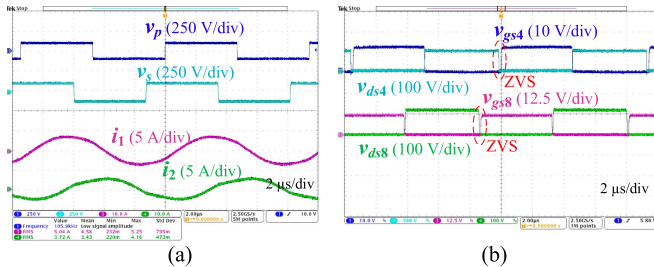


Fig. 20. Experimental steady-state waveforms with $g = 1.2, P_o = 400W$: (a) v_p, v_s, i_1 and i_2 ; and (b) $v_{gs4}, v_{ds4}, v_{gs8}, v_{ds8}$.

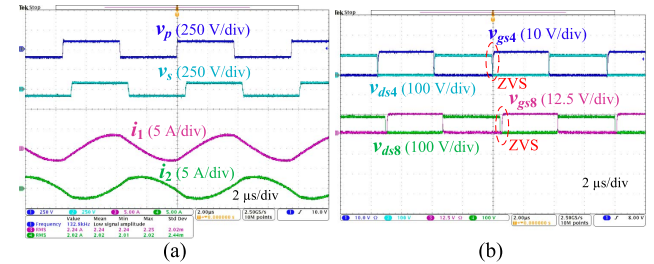


Fig. 21. Experimental steady-state waveforms with $g = 0.8, P_o = 100W$: (a) v_p, v_s, i_1 and i_2 ; and (b) $v_{gs4}, v_{ds4}, v_{gs8}, v_{ds8}$.

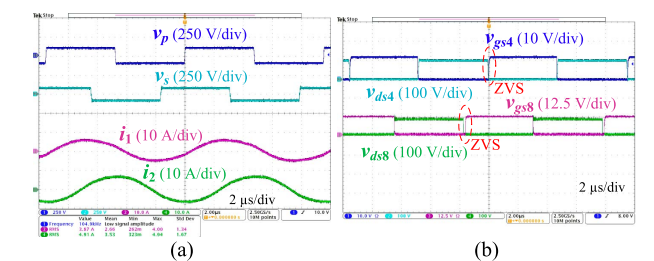


Fig. 22. Experimental steady-state waveforms with $g = 0.8, P_o = 300W$: (a) v_p, v_s, i_1 and i_2 ; and (b) $v_{gs4}, v_{ds4}, v_{gs8}, v_{ds8}$.

The calculated and experimental results on the rms current of TX and RX sides at $g = 1.0$ are shown in Fig. 23. As shown, experimental results agree well with the results predicted by our proposed method.

The efficiency with different modulation schemes is measured and plotted in Fig. 24. The conventional is the experimental results of a single phase shift at $r = 1.0$. As shown, the prototype demonstrates good efficiency performance over the wide output power range. The peak efficiency reaches 95.61% at full load. The proposed method has a better efficiency

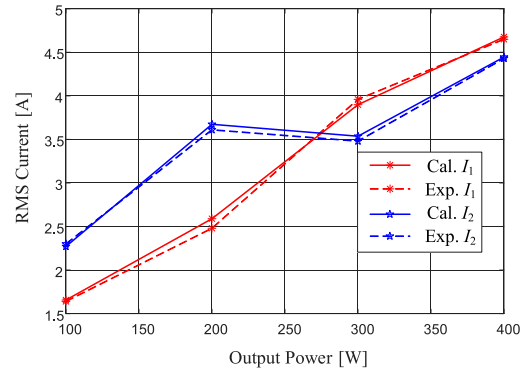


Fig. 23. Calculated and experimental results on rms current of TX and RX sides at $g = 1.0$.

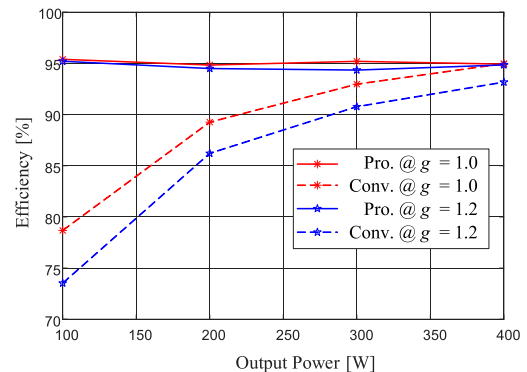


Fig. 24. Measured efficiency versus P_o with different modulation schemes.

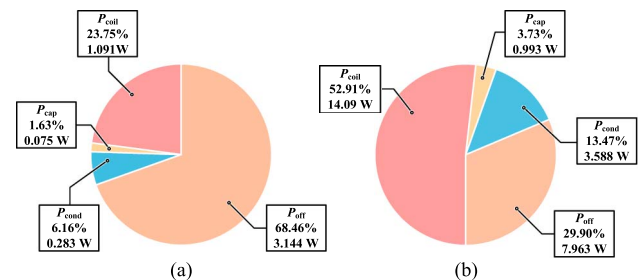


Fig. 25. Power loss distribution of system: (a) after optimization (total loss 4.591 W); and (b) before optimization (total loss 26.63 W).

performance compared with conventional fixed-frequency modulation schemes. Where $g = 1.0$, the loss distribution of power 100 W is shown in Fig. 25, this is mainly due to the reduced rms current and turn-OFF current. Thus, the conduction loss and switching loss are reduced, and the system efficiency is improved.

VI. COMPARISON WITH EXISTING WORK

To highlight the uniqueness and advantages of our state-plane-based frequency domain analysis for SS-compensated wireless power transfer, we compare it with four representative works [10], [21], [22], [23], addressing different modeling strategies and scenarios. A comprehensive comparison of the discussed methods is presented in Table V.

TABLE V
COMPARISON AMONG REPRESENTATIVE WORKS AND THIS ARTICLE

Reference	Method	Accuracy	Expandability	Complexity
Mohamed et al. [10]	Harmonic	Medium	Low	Low
Wang et al. [22]	Time-domain	High	Low	High
Jiao et al. [23]	Time-domain	High	Low	High
Rezayati et al. [21]	State-plane	High	Low	Medium
This Work	State-plane + Fourier	High	High	Low

A. Method Perspective

Mohamed et al. [10] use a steady-state analytical model combined with harmonic analysis to study active/reactive power flow in EV WPT systems. However, their approach lacks detailed time-domain analysis, especially concerning switching stresses.

Wang et al. [22] focus on multimode time-domain analysis and synchronous rectification (SR) strategies for *CLLC* converters under light-load conditions, accurately determining SR turn-ON timing. Despite the high accuracy for specific topologies and conditions, this method is less applicable to generalized networks.

Jiao et al. [23] apply the superposition harmonic method to analyze *CLLC* converters, considering multiple operating modes like ARFM and BRFM. This achieves precise *ZVS* ranges and switching stress calculations but relies heavily on piecewise time-domain modeling and focuses specifically on the *CLLC* topology.

Rezayati et al. [21] propose a generalized state-plane analysis (GSPA), decomposing the fourth-order *CLLC* system into two second-order subsystems. It provides high precision in CCM/DCM boundaries and *ZVS* conditions yet remains focused on the *CLLC* structure.

Our methodology combines state-plane decoupling with Fourier series expansion, facilitating simultaneous time-domain trajectory acquisition and harmonic amplitude/phase extraction. This dual approach enables accurate determination of switch turn-OFF currents and *ZVS* ranges, suitable for comprehensive IPT system analysis across various loads and frequencies.

B. Method Accuracy

Compared to conventional FHA methods [10], existing techniques improve prediction accuracy but still face challenges with light-load distortion or significant harmonics. Works [22], [23] achieve high-experimental accuracy through detailed piecewise time-domain derivations for specific conditions.

Our SPA with Fourier decomposition allows precise determination of harmonic currents/voltages' amplitude and phase, maintaining high accuracy across diverse operating conditions and predicting switching current waveforms and *ZVS* ranges, validated by experimental results.

C. Method Expandability

While Mohamed et al. [10] focus on EV WPT systems with fixed topologies, the authors [21], [22], [23] investigate *CLLC* converters requiring modifications for different compensation structures.

Our proposed method can be universally applied as long as the coupling matrix is diagonalizable. Thus, the original coupled

network can be decomposed into multiple SRC equivalent sub-networks. This characteristic enables analysis of various IPT scenarios, including SS/SP/PS/LCC compensation.

D. Method Complexity

Time-domain methods [22], [23] are accurate but involve extensive piecewise differential equations. Decoupling transformations [21] simplify *CLLC* analysis but use complex decoupling methods. Our method constructs a system matrix that, after linear transformation and decoupling, uses state-plane descriptions with Fourier series expansion to obtain harmonic parameters and switching conditions without additional piecewise integration, offering more compact and intuitive formulas.

In summary, the proposed method combines high-modeling accuracy and harmonic analysis capability with enhanced generality and reduced analytical complexity. The experimental results in Section V validate its effectiveness and precision. This approach offers a unified, efficient framework for modeling, analyzing, and optimizing design across a broad spectrum of IPT system applications.

VII. CONCLUSION

In this article, a novel state-plane-based frequency domain method is proposed for SS-compensated IPT systems. Through a series of matrix calculations, the coupled current on the TX and RX sides are decoupled into two independent components. Two decoupled equivalent circuits and corresponding state planes are established. The amplitude and phase information of each harmonics is obtained by the Fourier series expansion of current. The *ZVS* range is analyzed quantitatively. The efficiency is improved by optimizing the parameter design to reduce the rms values while ensuring *ZVS* is achieved. A 400 W-rated prototype is designed to verify its effectiveness and feasibility. The peak efficiency is measured as 95.61%. All switches achieve *ZVS* turn-ON at the full load range.

REFERENCES

- [1] J.-Q. Zhu, Y.-L. Ban, R.-M. Xu, and C. C. Mi, "An NFC-connected coupler using IPT-CPT-combined wireless charging for metal-cover smartphone applications," *IEEE Trans. Power Electron.*, vol. 36, no. 6, pp. 6323–6338, Jun. 2021.
- [2] O. Knecht and J. W. Kolar, "Performance evaluation of series-compensated IPT systems for transcutaneous energy transfer," *IEEE Trans. Power Electron.*, vol. 34, no. 1, pp. 438–451, Jan. 2019.
- [3] H. Jung and B. Lee, "Wireless power and bidirectional data transfer system for IoT and mobile devices," *IEEE Trans. Ind. Electron.*, vol. 69, no. 11, pp. 11832–11836, Nov. 2022.
- [4] E. S. Lee, "Frequency-modulation-based IPT with magnetic communication for EV wireless charging," *IEEE Trans. Ind. Electron.*, vol. 70, no. 2, pp. 1398–1408, Feb. 2023.

- [5] C. Cai, S. Wu, L. Jiang, Z. Zhang, and S. Yang, "A 500-W wireless charging system with lightweight pick-up for unmanned aerial vehicles," *IEEE Trans. Power Electron.*, vol. 35, no. 8, pp. 7721–7724, Aug. 2020.
- [6] Z. Chen, X. Zhang, F. Xu, M. Li, Z. Yuan, and Q. Yang, "Wide rotation-misalignment-tolerance design of magnetic coupled structure for AUVs wireless charging system," *IEEE Trans. Ind. Electron.*, vol. 71, no. 11, pp. 14086–14096, Nov. 2024.
- [7] B. Xue, L. Wang, M. Fu, and H. Wang, "State-space based universal time-domain model for voltage-fed bidirectional IPT systems," *IEEE Trans. Ind. Electron.*, vol. 71, no. 1, pp. 615–624, Jan. 2024.
- [8] H. L. Jou, J. C. Wu, K. D. Wu, and C. Y. Kuo, "Bidirectional DC-DC wireless power transfer based on LCC-C resonant compensation," *IEEE Trans. Power Electron.*, vol. 36, no. 2, pp. 2310–2319, Feb. 2021.
- [9] J. G. Kim, G. Wei, M. H. Kim, J. Y. Jong, and C. Zhu, "A comprehensive study on composite resonant circuit-based wireless power transfer systems," *IEEE Trans. Ind. Electron.*, vol. 65, no. 6, pp. 4670–4680, Jun. 2018.
- [10] A. A. Mohamed, A. Berzoy, and O. A. Mohammed, "Experimental validation of comprehensive steady-state analytical model of bidirectional WPT system in EVs applications," *IEEE Trans. Veh. Technol.*, vol. 66, no. 7, pp. 5584–5594, Jul. 2017.
- [11] A. Bucher and T. Duerbaum, "Analysis and design of a contactless power transmission system based on the extended first harmonic approximation," in *Proc. IEEE Ind. Appl. Soc. Annu. Meet.*, Oct. 2012, pp. 1–7.
- [12] Y. Fang and B. M. Pong, "Multiple harmonics analysis for variable frequency asymmetrical pulsewidth-modulated wireless power transfer systems," *IEEE Trans. Ind. Electron.*, vol. 66, no. 5, pp. 4023–4030, May 2019.
- [13] Y. Fang, B. M. Pong, and R. Hui, "An enhanced multiple harmonics analysis method for wireless power transfer systems," *IEEE Trans. Power Electron.*, vol. 35, no. 2, pp. 1205–1216, Jun. 2019.
- [14] A. Safaei and K. Woronowicz, "Time-domain analysis of voltage-driven series-series compensated inductive power transfer topology," *IEEE Trans. Power Electron.*, vol. 32, no. 7, pp. 4981–5003, Jul. 2017.
- [15] Y. Wei, Q. Luo, X. Du, N. Altin, J. M. Alonso, and H. A. Mantooth, "Analysis and design of the LLC resonant converter with variable inductor control based on time-domain analysis," *IEEE Trans. Ind. Electron.*, vol. 67, no. 7, pp. 5432–5443, Jul. 2020.
- [16] N. Shafiei, M. A. Sabet, and M. Ordonez, "Time domain analysis of LLC resonant converters in the boost mode for battery charger applications," in *Proc. IEEE Energy Convers. Congr. Expo. (ECCE)*, Oct. 2017, pp. 4157–4162.
- [17] X. Fang, H. Hu, Z. J. Shen, and I. Batarseh, "Operation mode analysis and peak gain approximation of the LLC resonant converter," *IEEE Trans. Power Electron.*, vol. 27, no. 4, pp. 1985–1995, Apr. 2012.
- [18] Z. Yang, J. Wang, H. Ma, and J. Du, "A wide output voltage LLC series resonant converter with hybrid mode control method," in *Proc. IEEE 2nd Int. Future Energy Electron. Conf. (IFEEC)*, Nov. 2015, pp. 1–5.
- [19] D. Biadene and G. Spiazzi, "A matrix presentation of state-plane analysis for a broad class of series-resonant converters," *IEEE Trans. Power Electron.*, vol. 33, no. 12, pp. 10935–10945, Jun. 2018.
- [20] J. Zhao, L. Wu, H. Lin, X. Sun, and G. Chen, "State trajectory control of burst mode for LCC resonant converters with capacitive output filter," *IEEE Trans. Power Electron.*, vol. 37, no. 1, pp. 377–391, Jan. 2022.
- [21] M. Rezaayati, F. Tahami, J.-L. Schanen, and B. Sarrazin, "Generalized state-plane analysis of bidirectional CLLC resonant converter," *IEEE Trans. Power Electron.*, vol. 37, no. 5, pp. 5773–5785, May 2022.
- [22] Y. Wang, B. Zhang, C. Liu, J. Tian, and F. Wang, "A precise time-domain multi-mode synchronous rectification strategy for CLLC resonant converters under light-load conditions," in *Proc. CPSS; IEEE ISESC*, 2024, pp. 534–537.
- [23] L. Jiao, L. Li, C. Wang, S. Zhang, B. Liu, and X. Fang, "High-precision time-domain analysis method based on the superposition principle for CLLC converter in above-resonant-frequency mode," *IEEE Trans. Power Electron.*, vol. 39, no. 11, pp. 14550–14564, Nov. 2024.



Yihan Wu (Student Member, IEEE) received the B.S. degree in electronic engineering in 2023 from ShanghaiTech University, Shanghai, China, where he is currently working toward the master's degree in electronic science and technology with the School of Information Science and Technology.

His research includes dc–dc converters, inductive power transfer systems, and resonant converters.



Bo Xue received the B.S. degree in electrical engineering and automation from Hefei University of Technology, Xuancheng, China, in 2017, and the Ph.D. degree in microelectronics and solid-state electronics from the Chinese Academy of Sciences, Shanghai Institute of Microsystem and Information Technology, Shanghai, China, in 2024.

He was a Graduate Research Assistant with the Power Electronics and Renewable Energies Laboratory, School of Information Science and Technology, ShanghaiTech University, Shanghai, from 2018 to 2024. Currently, he is a Power Hardware Engineer with Shenzhen Inovance Technology Co., Ltd., Shenzhen, China. His research interests include dc/dc converters, inductive power transfer, and resonant converters.



Junrui Liang (Senior Member, IEEE) received the Ph.D. degree in mechanical and automation engineering from The Chinese University of Hong Kong (CUHK), Hong Kong, China, in 2010.

In 2013, he joined the School of Information Science and Technology, ShanghaiTech University, where he is currently an Associate Professor. His research interests include dynamics of nonlinear electromechanical coupling systems, kinetic energy harvesting and vibration control, electrical power conversion and utilization research, and renewable energy.



Minfan Fu (Senior Member, IEEE) received the B.S., M.S., and Ph.D. degrees in electrical and computer engineering from the University of Michigan Shanghai Jiao Tong University Joint Institute, Shanghai Jiao Tong University, Shanghai, China, in 2010, 2013, and 2016, respectively.

He is currently an Associate Professor with the School of Information Science and Technology, ShanghaiTech University, Shanghai, China. From 2016 to 2018, he was a Postdoctoral Researcher with the Center for Power Electronics Systems (CPES), Virginia Polytechnic Institute and State University, Blacksburg, VA, USA. His research interests include megahertz wireless power transfer, high-frequency power conversion, high-frequency magnetic design, and the application of wide bandgap devices.



Haoyu Wang (Senior Member, IEEE) received the bachelor's (Distinguished Hons.) degree from Zhejiang University, Hangzhou, China, in 2009, and the Ph.D. degree from the University of Maryland, College Park, MD, USA, in 2014, both in electrical engineering.

In 2014, he joined the School of Information Science and Technology, ShanghaiTech University, where he is currently a Full Professor with tenure. In 2023, he was a Visiting Academic Fellow with the University of Cambridge, Cambridge,

U.K. His research interests include power electronics, electric vehicles, renewable energy systems, and power management integrated circuits.

Dr. Wang is an IET Fellow. He serves as an Associate Editor of *IEEE TRANSACTIONS ON INDUSTRIAL ELECTRONICS*, *IEEE TRANSACTIONS ON TRANSPORTATION ELECTRIFICATION*, and *CPSS Transactions on Power Electronics and Applications*. He was a Guest Editor of *IEEE JOURNAL OF EMERGING AND SELECTED TOPICS IN POWER ELECTRONICS* and a Guest Associate Editor of *IEEE TRANSACTIONS ON POWER ELECTRONICS*.